Miranda Pedro, M. A. (Orcid ID: 0000-0002-4288-9456)

Mateus Pedro, Jorge Belé (Orcid ID: 0000-0001-8027-2142)

Nico Giovanni (Orcid ID: 0000-0001-7621-5014)

Catalao Joao (Orcid ID: 0000-0003-1028-4644)

Tomé Ricardo (Orcid ID: 0000-0003-0657-7057)

Nogueira Miguel (Orcid ID: 0000-0003-4587-875X)

InSAR Meteorology: High-resolution Geodetic Data Can Increase Atmospheric Predictability

P.M.A. Miranda[1], P. Mateus[1†], G. Nico[2,3], J. Catalão[1], R. Tomé[1], and M. Nogueira[1]

[1]Instituto Dom Luiz (IDL), Faculdade de Ciências, Universidade de Lisboa, 1749-016 Lisboa, Portugal.

[2]Istituto per le Applicazioni del Calcolo (IAC), Consiglio Nazionale delle Ricerche (CNR), 70126 Bari, Italy.

[3]Institute of Earth Sciences, Saint Petersburg State University (SPSU), 199034 Saint Petersburg, Russia.

Corresponding author: Pedro Mateus (pjmateus@fc.ul.pt)

†Current address, Lisbon, Portugal.

Key Points:

- Assimilation of Synthetic Aperture Radar Interferograms consistently extends the skill of hindcasts of water vapor and precipitation
- A large fraction of forecast rain errors is due to errors in the distribution of water vapor
- The near-range forecast of heavy precipitation events may be substantially improved with better initial states of water vapor

This article has been accepted for publication and undergone full peer review but has not been through the copyediting, typesetting, pagination and proofreading process which may lead to differences between this version and the Version of Record. Please cite this article as doi: 10.1029/2018GL081336

Abstract

The present study assesses the added value of high-resolution maps of Precipitable Water Vapor (PWV), computed from Synthetic Aperture Radar Interferograms (InSAR), in short-range atmospheric predictability. A large set of images, in different weather conditions, produced by Sentinel-1A in a very well monitored region near the Appalachian Mountains, are assimilated by the WRF model. Results covering more than 2 years of operation indicate a consistent improvement of the water vapor predictability up to a range comparable with the transit time of the air mass in the InSAR footprint, an overall improvement in the forecast of different precipitation events, and better representation of the spatial distribution of precipitation. This result highlights the significant potential for increasing short-range atmospheric predictability from improved high-resolution PWV initial data, which can be obtained from new high-resolution all-weather microwave sensors.

Plain Language Summary

Weather forecasts will never be perfect because our models are simplified representations of nature and our observations of the atmosphere are inaccurate. In this study we show, nevertheless, that it is possible to improve such forecasts by interpreting the atmospheric signals in spaceborne radar observations of the Earth surface, indicative of the distribution of water vapor. Better and more detailed maps of water vapor are found to lead to better forecasts not just of water vapor, but also of precipitation. A two and a half years assessment covering a wide range of weather conditions in a very well monitored region near the Appalachian Mountains, USA, suggests that the proposed methodology has a significant impact in the quality of the forecasts and could easily be implemented.

1 Introduction

Accurate weather forecasts at different ranges are critical for most human activities and have gained increased relevance in a world more vulnerable to extreme weather events and water shortages. The quality of the initial state in those forecasts is, of course, one of the key elements of their success, and its uncertainty is one of the reasons for the development of the modern ensemble forecast techniques (Bauer et al., 2015). The present study explores the possibility of further reducing the initial state uncertainty through the assimilation of a new source of very-high resolution Precipitable Water Vapor (PWV) data, obtained from Synthetic Aperture Radar Interferograms (InSAR).

In the absence of surface deformation, and after the mitigation of the ionospheric and hydrostatic phase signals (Hanssen, 2001; Wadge et al., 2002; Mateus et al., 2013a, 2013b; Kinoshita et al., 2013; Remy et al., 2015, Mateus et al., 2017), InSAR images can be used to compute the spatial distribution of PWV, offering one of the few data sources with a horizontal resolution relevant for the atmospheric mesoscale. Its impact in short-range numerical weather prediction (NWP) was recently assessed in three studies. Pichelli et al. (2015) found improvements in hindcasting weak to moderate precipitation (< 15 mm/3-h) in a three-dimensional variational (3D-Var) data assimilation of InSAR-PWV maps using the mesoscale weather prediction model MM5 and ENVISAT-ASAR data over the city of Rome, Italy. Mateus et. al. (2016) showed a significant improvement in the atmospheric moisture content, and on the formation of light precipitation up to 9 hours after the assimilation time in a 3D-Var data assimilation experiment using InSAR-PWV maps, estimated from the ENVISAT-ASAR data, and the Weather Research and Forecast (WRF) model over Lisbon,

Portugal. Mateus et al. (2018) showed that in a case with two successive deep convection storms, which could be both well forecasted only after InSAR data assimilation using two PWV maps estimated from new generation SAR images obtained by Sentinel-1 A over Adra, Spain, with the 3D-Var method and the WRF model. The latter result suggested the high potential added value of the new InSAR data, and the need for a systematic evaluation of its value in a representative range of weather conditions, which is the objective of the current study.

The availability of a high-quality gridded dataset of precipitation, and of a good network of GNSS observations, make the continental USA ideal testing ground for evaluation. The present work focuses on a subsector, near the Appalachian Mountains (cf. Figure 1), characterized by a humid continental climate with frequent precipitation events strongly modulated by the complex topography, resulting in high spatial and temporal variability (e.g., Nogueira and Barros, 2015). On the one hand, a significant fraction (30-50%) of its precipitation is associated with light rain from fog and low-level clouds (Wilson and Barros, 2014). On the other hand, this region is also often affected by strong precipitation events, often leading to flooding, debris flows and landslides (Tao and Barros, 2014). Furthermore, these intense events can have multiple origins, including the passage of cold season synoptic-storms and warm-season mesoscale convective systems, tropical depressions and localized convection. Here it is hypothesized that both light and heavy precipitation events should be sensitive to the detailed distribution of PWV. This region has a further advantage of having Sentinel-1A observations (at 23:45 UTC) almost synchronized with the main NWP analysis at 00 UTC, clearly separating the effect of the InSAR PWV data from other gains one might obtain from an update of the initial state and initial conditions in the middle of a simulation.

2 Data and Methods

2.1 InSAR data

Sentinel-1A operates a C-Band Synthetic Aperture Radar (SAR) producing very high-resolution imagery with a pixel of 5×20 m^2, returning to the same Earth view every 12 days. In each passage, the system can produce two images in the ascending (day side) and descending (night side) sides of its orbit. However, in the study area, only ascending images taken at about 23:45 UTC were generally available in the period from January 2016 to May 2018. Each Single Look Complex (SLC) image produced by the SAR covers a rectangle of about 170×255 km^2 in the chosen region. Two adjacent images along the flight pass were merged in a single interferogram for the present study following the method described in Mateus et al. (2017), covering a rectangle of about 340×255 km^2 as shown in Figure 1. Overall, 51 interferograms (maps of phase difference) were computed whenever possible from SAR images 12 days apart, or in the case of a missing image (19 cases) from images separated by 24 days by means of the Sentinel Application Platform (http://step.esa.int/main/toolboxes/snap/). A spatial multilook-filter was applied to reduce the phase noise, leading to InSAR interferograms with a resolution of about 350×350 m^2. Before applying the phase unwrapping algorithm, estimates of the ionospheric and hydrostatic components were subtracted keeping only the contribution due to the atmospheric water vapor. Areas with high spatial phase decorrelation (possibly due to water surfaces, 12-day changes in vegetation or anthropogenic activities) were masked out. After a visual analysis of the interferometric phase and coherence maps, a total of 6 interferograms were eliminated

from this study due to the high percentage of temporal decorrelation (mainly due to changes of the vegetation in summertime), leaving 45 interferograms for further analysis.

During the dataset time span, there were no relevant seismic events in the study area, so that the remaining interferometric phase includes only the atmospheric water vapor contribution. The unwrapped phase was converted in ΔPWV quantity using an adaptation of the formulation by Bevis (1992, 1994). These maps were calibrated with 4 Global Navigation Satellite System (GNSS) observations (white circles in Figure 1), to eliminate an arbitrary constant in the phase. Finally, the InSAR differential PWV maps were converted into absolute PWV maps using an estimate of the PWV distribution at the first simulated date, obtained by the same exercise on the earlier date using the same WRF model, following Mateus et al. (2018). Other comparable methods were proposed by Pichelli et al. (2015) and Alshawaf et al. (2015). The final maps, when compared against all available GNSS observations have a final root mean square error below 2 mm.

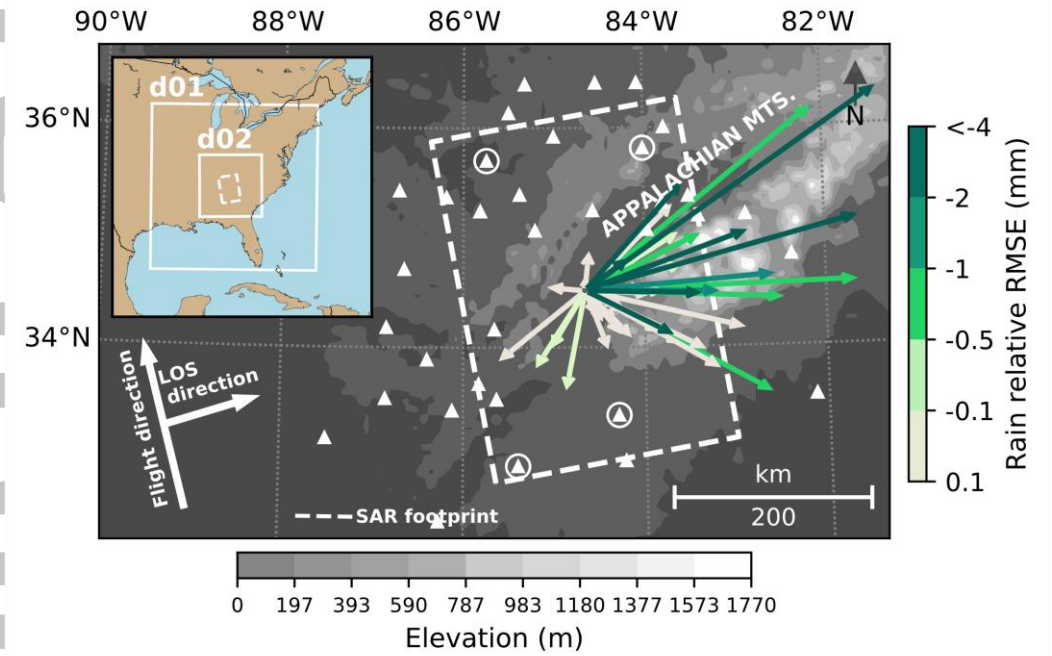

Figure 1. Study area: SAR footprint (dashed line rectangle); GNSS stations (white triangles, circles locate those used for calibration); domains of simulation (top left insert). Gray shading represents terrain elevation. Arrows represent the water vapor flux estimated as the product of 700 hPa wind by PWV for each of the 45 hindcast experiments. Arrow colors indicate the change in RMSE of accumulated rainfall in 12 h.

2.2 WRF model configuration

For the present study, the WRF model used exactly the setup described in Mateus et al. (2018), except the number, area, and dimension of the domains. In this case the model had two domains, the inner domain (d02 in Fig. 1) with 3 km horizontal resolution, covering longitudes 79.8˚ - 89.4˚ West and latitudes 30.5˚ - 38.2˚ North, and the parent domain (d01 in Fig. 1) with 9 km horizontal resolution covering longitudes 68.6˚ - 96.3˚ West and latitudes 24.3˚ - 44.7˚ North. The outer domain was forced by NCEP GFS boundary conditions.

2.3 Data assimilation

The 3D-Var data assimilation method (Barker et al., 2004) was used in this experiment. The first-guess error covariance matrix required by 3D-Var was computed by the National Meteorological Centre (NMC) method (Parrish and Derber, 1992), based on differences between forecasts at different ranges valid at the same time. Four full months (February, May, August and November 2017, sampling the annual cycle), were simulated offline to compute the first-guess error covariance. For the observation covariance error matrix, the default value of 2 mm in the 3D-Var PWV assimilation scheme was adopted to represent all sources of error. The WRF Data Assimilation (WRFDA) package was used with default options, except for the use of a smaller distance (15 km) in the "thinning" algorithm, which samples one datapoint from the 350 m filtered InSAR data, in each 15×15 km^2 grid box to assimilate. This distance is a compromise to maintain the assumption that the observations are statistically independent in space, as required by the 3D-Var scheme, and was successfully tested in Mateus et al. (2018).

Two sets of 45 experiments were made, the control (CTRL) run starting at 1800 UTC and running for 30 hours, and then a 24-hour A-InSAR run, which uses the output of CTRL at 0000 UTC (after a 6-hour spin-up) as first-guest to assimilate the PWV data (valid at 23:45 UTC) into new initial conditions.

3 Results

Results from the 45 simulation pairs (corresponding to CTRL and A-InSAR, for each of 45 available interferograms) will now be assessed against two sets of independent observations: hourly time series of PWV estimated by 41 GNSS stations (from the CORS and SuomiNet networks), and Stage IV, a merged gauge-radar gridded precipitation dataset at 4 km resolution covering the continental USA, obtained from the National Oceanic and Atmospheric Administration (NOAA) National Centers for Environmental Prediction (NCEP) (Lin and Mitchell, 2005; Nelson et al., 2016). GNSS PWV measures both the temporal and spatial behavior of the simulations, in a smooth continuous and slowly varying column integrated water vapor, in relatively coarse columns a few tens of kilometers across. Here Stage IV precipitation is summed over each 12-hour period (from 6-hour data) allowing the evaluation of fine spatial detail, while avoiding (by time averaging) the problems coming from slight errors in the storm's propagation speed across the domain.

For each of the 45 hindcast experiments, the CTRL and A-InSAR simulations were compared, using a two-tailed t-test (Snedecor and Cochran, 1989). For that purpose, each dataset was characterized by 100 regularly spaced and co-located grid points within the InSAR area. The null hypothesis assumed that both datasets were statistically equal, i.e. drawn from the same distribution, and the alternative hypothesis that they were statistically different. The test was applied every hour after the assimilation time, at the 0.05 significance level until a null hypothesis was accepted. In 15 simulation pairs, the null hypothesis was accepted at assimilation time (hour 0) indicating that InSAR data didn't impact that particular forecast and suggesting that the corresponding initial state was already well established in the CTRL simulation. The remaining 30 simulations were assessed for as long as the statistical test found CTRL and A-InSAR significantly different.

The PWV RMSE of both CTRL and A-InSAR, computed against GNSS observations, indicates that all 30 A-InSAR simulations had a better match with observations (smaller RMSE) while the statistical test rejected the null hypothesis (cf. Supplementary Figure S1

and S2), translating to a straightforward conclusion of extended skill associated with each A-InSAR simulation. That extension in skill was found to be limited, but close, to the transit time of the air mass over the InSAR footprint, as shown by the dashed line in Figure 2. The transit time of the air mass was estimated from the mean 700 hPa velocity at assimilation time, which was taken as its steering level. Almost all cases show an increase in skill above half of the transit time (dash-dotted line). The spatial distribution of the 700 hPa velocity and the corresponding uncertainty in the transit time (horizontal error bars in Figure 2) are elaborated in Supplementary Figure S3.

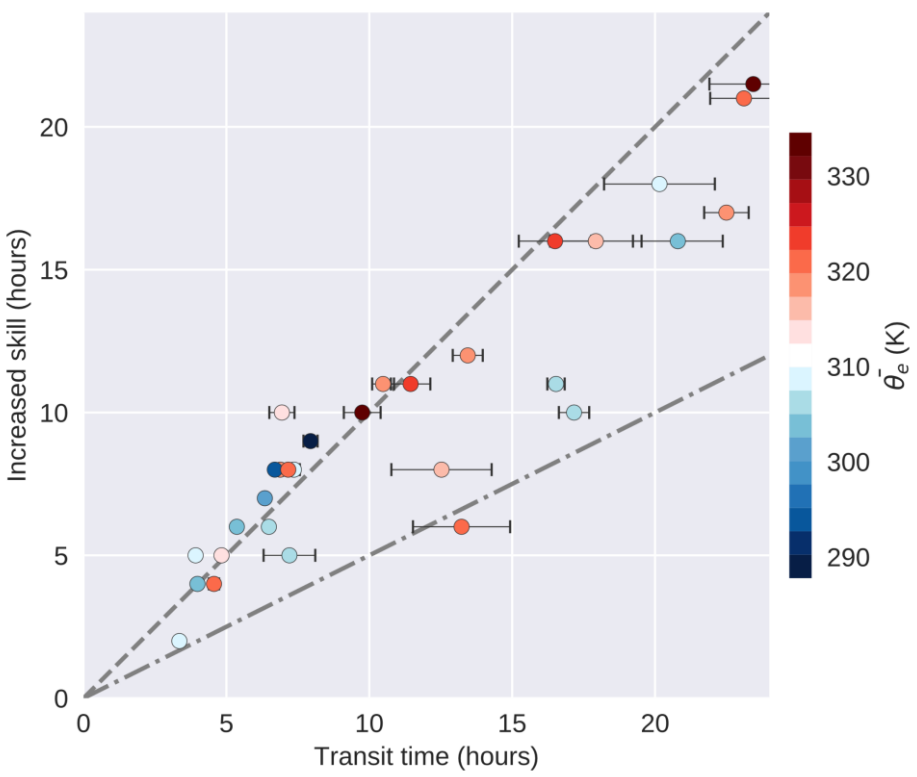

Figure 2. Duration of increased skill (in hours) vs. air mass transit time (in hours), for the 30 cases sensitive to the change in initial state. The color shading shows the mean equivalent potential temperature (in Kelvin) at 700 hPa level over the InSAR window indicating a combination of warmth and moisture of the airmass. Individual simulations analyzed in Figure S1, S2 and S3.

Precipitation is, for most applications, a more crucial variable than PWV, but harder to forecast since it depends on both thermodynamic and dynamic constrains and is characterized by strong intermittency in space and time. The 12 h-mean assessment of the spatial skill of precipitation shown in Figure 1 indicates a reduction in its RMSE in most experiments, with largest improvements in the cases characterized by strong horizontal water vapor flux carried by tropical airmasses coming from SW. This is consistent with the fact that many experiments with largest improvements of the forecast skill in Figure 2 have high values of equivalent potential temperature.

The time-mean solution of all simulations, representing a sample of the precipitation climate in the region, is analyzed in Figure 3, comparing the two sets of simulations (CTRL and InSAR) against observations (Stage IV). CTRL clearly underestimates the frequency of drier, and strongly overestimates the frequency of wetter patches. The distribution of

precipitation in A-InSAR is much closer to observations, with the values of the 4 first statistical moments (mean, variance, skewness and kurtosis) all approaching the respective values in the observations. One should keep in mind that Stage IV, although calibrated against point udometer data, is affected by inherent biases in radar estimation, particularly over mountainous regions (Nelson et al., 2016). Similarly, WRF simulations are affected by shortcomings in parametrization schemes. The result presented in Figure 3 strongly suggests, however, that a large fraction of WRF errors are due to errors in the initial distribution of water vapor.

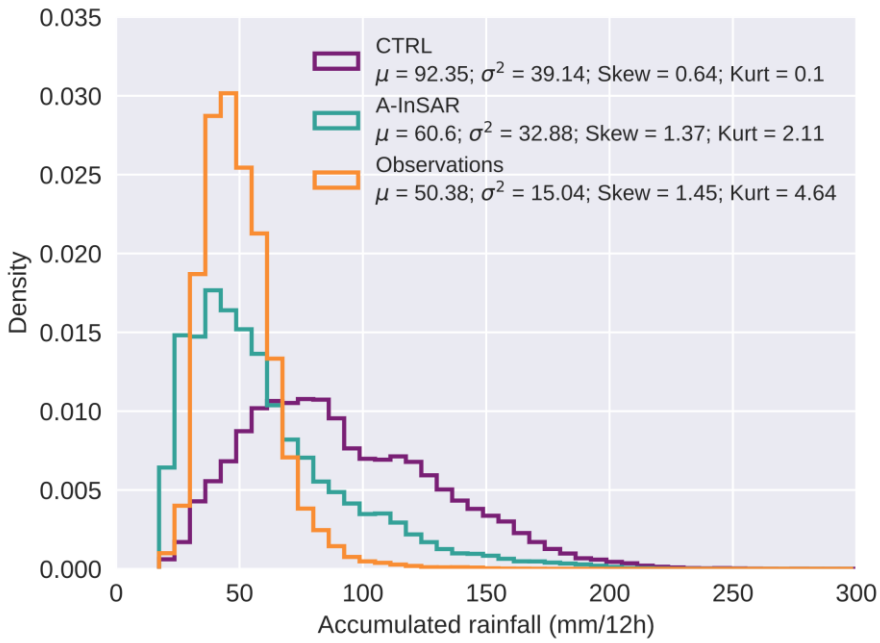

Figure 3. Histogram of the CTRL, A-InSAR and observed (Stage IV) time average rainfall fields. Estimates of the mean, variance, skewness, and kurtosis also shown.

Because precipitation varies dramatically between meteorological events, with a large majority of no-rain and light-rain conditions and a small number of heavy rain events, it is important to check how the forecast performs in the identification of different precipitation classes. Using 12 hour accumulated fields, contingency tables were computed for both CTRL and A-InSAR against Stage IV observations, for 4 classes of accumulated precipitation: no-rain ($R<0.1$ mm), light rain ($0.1 \leq R<10$ mm), moderate rain ($10 \leq R<30$ mm), and heavy rain ($R \geq 30$ mm). An analysis of the mismatch is presented in Table 1, where it is clear that the assimilation of InSAR data increased the Hit-rate (fraction of rightly forecasted events, Percent Correct) and reduced the misses. Misses by three-classes (forecasting heavy precipitation with no-rain observed, or the other way round) were reduced by a factor of 5 (from 0.5% to 0.1%), misses by two-classes were reduced by a factor of 1.5 (from 1.8% to 1.2%), misses in the adjacent class were only slightly reduced (from 17.2% to 15%). A look into the details of the contingency tables (supplementary material Figure S3) indicates that most gains come from a reduction in the overestimation of heavy and moderate rain events, in cases with no or light observed rain. As shown in Figure S4, the gains obtained in the forecast of observed light and no-rain events, are slightly compensated by a very small increase in the forecast of no and light-rain, in cases where heavy rain was observed.

Table 1. Hit and miss from 4 class rain contingency table (see Figure S2). Relative improvement is defined as the ratio between InSAR and CTRL (hit) or between CTRL and InSAR (miss).

		CTRL	A-InSAR	Relative Improvement
Percent Correct		80.5%	83.7%	1.04
miss	by 1 class	17.2%	15.0%	1.15
	by 2 classes	1.8%	1.2%	1.50
	by 3 classes	0.5%	0.1%	5.00

4 Discussion and conclusions

The region near the Appalachians offers favorable conditions to test the potential impact of high-resolution InSAR water vapor data: it is one of the best monitored regions in the world, with an already very good operational forecast, frequent rain, and with a synchronization of Sentinel-1 A images with the timing of the main meteorological analysis and forecast. The full already available dataset of those images constitutes a set of cases covering different meteorological conditions, in the different seasons. In about 2/3 of the simulated cases, InSAR was found to improve the forecast, with negligible impact in the remaining 1/3 (where the InSAR-derived PWV field was already very similar to analysis). Improvements were found in both the forecast skill of PWV, evaluated every hour in 41 GNSS stations, and in different metrics of 12 h accumulated precipitation error evaluated against the Stage IV gridded precipitation product.

Simulations made with InSAR data assimilation showed an improved forecast skill up to 24 h after assimilation time, with the skill improvement being limited (but close) to the estimated time taken by the air mass to cross the InSAR footprint. This implies that the forecast of slowly moving air masses benefits for a longer time from the improved initial state and suggests that it could be possible to generally improve the forecast if the images had a wider along flow extent. The improvement translated in a much better precipitation climate, as represented by the histogram of mean precipitation, a better spatial distribution of 12 h accumulated precipitation shown by a lower RMSE, and more importantly a clear improvement of the forecast Hit rate of different precipitation classes, especially a large relative reduction of the worst miss rates.

These results show a strong case for the assimilation of InSAR data in weather forecasts, bolstering a few specific case studies of some severe deep-convection events (Mateus et al., 2018). The relatively large sample of cases evaluated here suggest that such gains were not fortuitous, but a consistent response to an improved initial state, valid in different weather conditions. There is, however, the need to explore the method in other geographical settings and with other global forcing, as some of the improvements shown here may be compensating for specific biases at the chosen location in GFS initial fields. On the other hand, the result shown in Figure 3 suggests that this approached may be useful to identify some of those biases. It is important to mention, however, that the assimilation of InSAR PWV data is not just compensating for a wet bias in the GFS forecast. Indeed, Supplementary Figure S5 shows that gains in skill were obtained for initial states that were either too wet or too dry, in comparable numbers. On the other hand, Supplementary Figure

S6 indicates that the data assimilation modified the water vapor profile in the lower troposphere, with a maximum mean impact near 850 hPa, where both positive and negative increments were taken in different days, with only a very slight average drying effect (about -0.2 g/kg at 850 hPa).

InSAR meteorology has the potential to become a rapidly developing field. It is a global and all-weather product, available at resolutions relevant for the atmospheric mesoscale. For InSAR to be integrated into operational forecasts, however, it needs, real-time delivery, ideally for shorter time differences at least daily updates over the same Earth view. By combining Sentinel-1A/B and ascending plus descending orbits, it is now possible to obtain images every 6 days, if all images are acquired (which has been the case only over Europe). A number of proposed Radar platforms may fill the gaps, once they are deployed.

Acknowledgments

This work was supported by the Fundação para a Ciência e a Tecnologia (FCT), Portugal, under Postdoctoral grant SFRH/BPD/96069/2013, by FCT-Instituto Dom Luiz under Project UID/GEO/50019/2013 and by the Ministero dell'Istruzione, dell'Università e della Ricerca (MIUR), Italy, under the project OT4CLIMA. GNSS data are available from the network of Continuously Operating Reference Stations (CORS) in https://www.ngs.noaa.gov/CORS/ and from the SuomiNet network in https://www.suominet.ucar.edu/data.html. The Sentinel-1A SAR images are available from the Copernicus Open Access Hub in https://scihub.copernicus.eu/. NCEP Stage IV precipitation data are available from https://rda.ucar.edu/datasets/ds507.5/. Weather model dataset used in this study is available from the figshare repository (doi:10.6084/m9.figshare.7352219). We are indebted to the National Centers for Environmental Prediction (NCEP) for granting access to their products; data are available from the NCAR products inventory (http://www.nco.ncep.noaa.gov/pmb/products/gfs/). Suggestions made by Brian Mapes (University of Miami) and one anonymous referee contributed to improve this paper.

References

Alshawaf, F., Hinz, S., Mayer, M., & Meyer, F. J. (2015). Constructing accurate maps of atmospheric water vapor by combining interferometric synthetic aperture radar and GNSS observations. *Journal of Geophysical Research: Atmospheres*, 120, 1391–1403. https://doi.org/10.1002/2014JD022419

Barker, D. M., Huang, W., Guo, Y.-R., Bourgeois, A. J., & Xiao, Q. N. (2004). A three-dimensional variational data assimilation system for MM5: Implementation and initial results. *Monthly Weather Review*, 132, 897-914. https://doi.org/10.1175/1520-0493(2004)132<0897:ATVDAS>2.0.CO;2

Bauer, P., Thorpe, A., & Brunet, G. (2015). The quiet revolution of numerical weather prediction. *Nature*, 525, 47-55. https://doi.org/10.1038/nature14956

Bevis, M., Businger, S., Chiswell, S., Herring, T., Anthes, R., Rocken, C., & Ware, R. (1994). GPS meteorology: Mapping zenith wet delays onto precipitable water. *Journal of Applied Meteorology*, 33(3), 379–386. https://doi.org/10.1175/15200450(1994)033<0379:GMMZWD>2.0.CO;2

Bevis, M., S. Businger, T. A. Herring, C. Rocken, R. A. Anthes, & R. H. Ware. (1992). GPS meteorology: Remote sensing of atmospheric water vapor using the global positioning system. *Journal of Geophysical Research*, 97(D14), 15787-15801, https://doi.org/10.1029/92JD01517

Hanssen, R. (2001). Radar interferometry: Data interpretation and error analysis, remote sensing and digital image processing (1st ed., Vol. 2). Netherlands: Springer

Kinoshita, Y., Shimada, M., & Furuya, M. (2013). InSAR observation and numerical modeling of the water vapor signal during a heavy rain: A case study of the 2008 Seino event, central Japan. *Geophysical Research Letters*, 40, 4740-4744. https://doi.org/10.1002/grl.50891

Lin, Y., & Mitchell, K. E. (2005). The NCEP Stage II/IV hourly precipitation analysis: development and applications. In: 19th Conf. on Hydrology, American Meteorological Society, San Diego, CA, pp. 9-13

Mateus, P., Catalão, J., & Nico, G. (2017). Sentinel-1 interferometric SAR mapping of precipitable water vapor over a country-spanning area. *IEEE Transactions on Geoscience and Remote Sensing*, 55(5), 2993-2999. https://doi.org/10.1109/TGRS.2017.2658342

Mateus, P., Miranda, P. M. A., Nico, G., Catalão, J., Pinto, P., & Tomé, R. (2018). Assimilating InSAR maps of water vapor to improve heavy rainfall forecasts: A case study with two successive storms. *Journal of Geophysical Research: Atmospheres*, 123, 3341-3355. https://doi.org/10.1002/2017JD027472

Mateus, P., Nico, G., & Catalão, J. (2013a). Can spaceborne SAR interferometry be used to study the temporal evolution of PWV? *Atmospheric Research*, 119, 70–80. https://doi.org/10.1016/j.atmosres.2011.10.002

Mateus, P., Nico, G., Tomé, R., Catalão, J., & Miranda, P. M. A. (2013b). Experimental study on the atmospheric delay based on GPS, SAR interferometry, and numerical weather model data. *IEEE Transactions on Geoscience and Remote Sensing*, 51(1), 6–11. https://doi.org/10.1109/TGRS.2012.2200901

Mateus, P., Tomé, R., Nico, G., & Catalão, J. (2016). Three-dimensional variational assimilation of InSAR PWV using the WRFDA model. *IEEE Transactions on Geoscience and Remote Sensing*, 54(12), 7323-7330. https://doi.org/10.1109/TGRS.2016.2599219

Nelson, B. R., Prat, O. P., Seo, D. J., & Habib, E. (2016). Assessment and Implications of NCEP Stage IV Quantitative Precipitation Estimates for Product Intercomparisons. *Weather and Forecasting*, 31, 371–394. https://doi.org/10.1175/WAF-D-14-00112.1

Nogueira, M., & Barros, A. P. (2015). Transient stochastic downscaling of quantitative precipitation estimates for hydrological applications. *Journal of Hydrology*, 529(Part 3), 1407-1421. https://doi.org/10.1016/j.jhydrol.2015.08.041

Parrish, D. F., & Derber, J. C. (1992). The national meteorological center's spectral statistical-interpolation analysis system. *Monthly Weather Review*, 120(8), 1747–1763. https://doi.org/10.1175/1520-0493(1992)120<1747:TNMCSS>2.0.CO;2

Pichelli, E., Ferretti, R., Cimini, D., Panegrossi, G., Perissin, D., Pierdicca, N., et al. (2015). InSAR water vapor data assimilation into mesoscale model MM5: Technique and pilot study. *IEEE Journal of Selected Topics in Applied Earth Observations and Remote Sensing*, 8(8), 3859-3875. https://doi.org/10.1109/JSTARS.2014.2357685

Remy, D., Chen, Y., Froger, J. L., Bonvalot, S., Cordoba, L., & Fustos, J. (2015). Revised interpretation of recent InSAR signals observed at Llaima volcano (Chile). *Geophysical Research Letters*, 42, 3870-3879. https://doi.org/10.1002/2015GL063872

Skamarock, W. C., Klemp, J. B., Dudhia, J., Gill, D. O., Barker, D. M., Duda, M. G., Huang, X.-Y., Wang, W., & Powers, J. G. (2008). A Description of the Advanced Research WRF Version 3. NCAR Tech. Note NCAR/TN-475+STR, 113 pp. https://doi.org/10.5065/D68S4MVH

Tao, J., and Barros, A. P. (2014). Coupled prediction of flood response and debris flow initiation during warm- and cold-season events in the Southern Appalachians, USA. *Journal of Hydrology and Earth System Sciences*, 72, 367-388. https://doi.org/10.5194/hess-18-367-2014

Wadge, G., Webley, P. W., James, I. N., Bingley, R., Dodson, A., Waugh, S., et al. (2002). Atmospheric models, GPS and InSAR measurements of the tropospheric water vapour field over Mount Etna. *Geophysical Research Letters*, 29(19), 1905. https://doi.org/10.1029/2002GL015159

Wilks, D. (2011). Statistical methods in the atmospheric sciences, International Geophysics Series (3rd ed., Vol. 100). Academic Press. pp. 704

Wilson, A. M., & Barros, A. P. (2014). An Investigation of Warm Rainfall Microphysics in the Southern Appalachians: Orographic Enhancement via Low-Level Seeder–Feeder Interactions. *Journal of the Atmospheric Sciences*, 71, 1783-1805. https://doi.org/10.1175/JAS-D-13-0228.1